ARL-TR-10226 ● Nov 2025

Exploring High-Energy and High-Power Density Silicon-Anode Batteries for UAS Applications Under Extreme Operating Conditions

by Soojin Park, Sungho Kim, Dong-Yeob Han, Jaeho Jung, and Chol-Bum M. Kweon

DISTRIBUTION STATEMENT A. Approved for public release: distribution unlimited.

NOTICES

Disclaimers

The findings in this report are not to be construed as an official Department of the Army position unless so designated by other authorized documents.

Citation of manufacturer's or trade names does not constitute an official endorsement or approval of the use thereof.

Destroy this report when it is no longer needed. Do not return it to the originator.

ARL-TR-10226 ● Nov 2025

Exploring High-Energy and High-Power Density Silicon-Anode Batteries for UAS Applications Under Extreme Operating Conditions

Soojin Park, Sungho Kim, Dong-Yeob Han, and Jaeho Jung
Pohang University of Science and Technology

Chol-Bum M. Kweon
DEVCOM Army Research Laboratory

DISTRIBUTION STATEMENT A. Approved for public release: distribution unlimited.

REPORT DOCUMENTATION PAGE

1. REPORT DATE	2. REPORT TYPE	3. DATES COVERED	
		START DATE	END DATE
November 2025	Technical Report	15 September 2023	6 September 2025

4. TITLE AND SUBTITLE
Exploring High-Energy and High-Power Density Silicon-Anode Batteries for UAS Applications Under Extreme Operating Conditions

5a. CONTRACT NUMBER	5b. GRANT NUMBER	5c. PROGRAM ELEMENT NUMBER
FA520923C0024		
5d. PROJECT NUMBER	**5e. TASK NUMBER**	**5f. WORK UNIT NUMBER**

6. AUTHOR(S)
Soojin Park, Sungho Kim, Dong-Yeob Han, Jaeho Jung, and Chol-Bum M. Kweon

7. PERFORMING ORGANIZATION NAME(S) AND ADDRESS(ES)
Pohang University of Science and Technology
ATTN: POSTECH
Pohang, Kyungbuk, South Korea

8. PERFORMING ORGANIZATION REPORT NUMBER
ARL-TR-10226

9. SPONSORING/MONITORING AGENCY NAME(S) AND ADDRESS(ES)	10. SPONSOR/MONITOR'S ACRONYM(S)	11. SPONSOR/MONITOR'S REPORT NUMBER(S)
DEVCOM International Technology Center Pacific ATTN: USAITC-PAC-JA Tokyo, Japan		

12. DISTRIBUTION/AVAILABILITY STATEMENT
DISTRIBUTION STATEMENT A. Approved for public release: distribution unlimited.

13. SUPPLEMENTARY NOTES
ORCID: Chol-Bum M. Kweon, 0000-0002-3666-9406

14. ABSTRACT
This study optimized silicon (Si)-anode lithium-ion batteries for unmanned aircraft systems (UASs), focusing on high discharge rates and low-temperature performance. Cathode and anode materials, electrolytes, and electrode architecture were refined using CR2032 coin cells and validated with pouch cells. Lithium iron phosphate was selected for its superior capacity retention, and 15 wt% Si was identified as the optimal anode composition. A localized high-concentration electrolyte (LDBFT 13311) with 5 wt% vinylene carbonate and chemical vapor deposition-deposited Si enhanced stability and scalability. Despite outperforming existing Si-anode technologies at –20 °C, capacity retention was limited to 28%, requiring thermal management for UAS viability. The battery is best suited for hybrid electric propulsion systems with short-duration high discharge rates and cold exposure.

15. SUBJECT TERMS
UAS, power density, energy density, high discharge rate, low-temperature performance, silicon anode, localized high-concentration electrolyte, hard carbon, chemical vapor deposition silicon, thermal management, hybrid electric, Energy Sciences

16. SECURITY CLASSIFICATION OF:			17. LIMITATION OF ABSTRACT	18. NUMBER OF PAGES
a. REPORT	b. ABSTRACT	C. THIS PAGE		
UNCLASSIFIED	UNCLASSIFIED	UNCLASSIFIED	UU	37

19a. NAME OF RESPONSIBLE PERSON	19b. PHONE NUMBER *(Include area code)*
Chol-Bum M. Kweon	(520) 691-5909

STANDARD FORM 298 (REV. 5/2020)
Prescribed by ANSI Std. Z39.18

Contents

List of Figures

1. Introduction

The rapid advancement of unmanned aircraft systems (UASs) has profoundly impacted numerous fields, including military operations. These UASs, which are becoming increasingly integral to a wide range of applications, require robust energy solutions to meet growing demands for endurance, payload capacity, and operational range.[1] The energy systems that power UASs must not only deliver high-energy density to enable extended flight durations but must also maintain reliable performance under extreme conditions, such as the low temperatures encountered at high altitudes and in cold regions.

Lithium-ion batteries (LIBs) have become the cornerstone of portable energy storage due to their high-energy density, long cycle life, and relatively low self-discharge rates.[2] These characteristics make LIBs highly suitable for a wide range of applications, including consumer electronics, electric vehicles, and small drones. However, low-temperature environments pose a significant challenge for LIBs, as they result in increased internal resistance, reduced ionic conductivity, and a marked decline in electrochemical reaction rates—particularly under high charge or discharge conditions. These effects collectively lead to a substantial reduction in battery performance, evidenced by diminished capacity, lower power output, and accelerated degradation.

This challenge has prompted extensive research into the development of advanced active materials and electrolytes capable of overcoming the performance limitations commonly observed in conventional LIBs under subzero temperatures and high-discharge conditions. The active materials in LIBs play a critical role in storing and releasing energy during charge and discharge cycles, and their behavior significantly influences overall battery performance in low-temperature environments.[3] To ensure overall battery efficiency and longevity, anode and cathode materials must demonstrate high capacity, stability, and conductivity, even under low-temperature conditions.

Among these, the anode material plays a particularly critical role in determining battery performance in cold environments. Although graphite anodes are widely used, they exhibit notable limitations, including susceptibility to lithium metal plating and diminished performance at subzero temperatures. To overcome these challenges, recent research has focused on developing composite anodes that integrate hard carbon (HC) and silicon (Si). HC, a non-graphitizable form of carbon, is especially valued for its structural stability and ability to maintain consistent performance across a wide temperature range.[4] Unlike graphite, HC possesses a disordered structure with larger interlayer spacing and a high density of

defects,[5] which facilitates lithium-ion intercalation even at lower temperatures. Si, by contrast, offers a significantly higher theoretical capacity than graphite, making it a promising candidate for enhancing the energy density of LIBs. However, its considerable volume expansion during lithiation and delithiation presents a major challenge, often resulting in mechanical degradation and the loss of electrical contact within the electrode.[6] HC serves as a stable framework that accommodates the expansion and contraction of Si, thereby enhancing the structural integrity and low-temperature performance of the anode.[7] An optimized composite anode, featuring a carefully balanced ratio of HC to Si, is expected to deliver improved functionality in subzero environments, sustaining high capacity while minimizing degradation. This synergistic interaction between materials enables the battery to maintain high output even under demanding environmental conditions.

The cathode material plays an equally critical role in determining a battery's overall performance, particularly its power output and stability under low-temperature conditions. Major cathode materials include lithium iron phosphate (LFP) and nickel manganese cobalt oxide (NMC). Traditionally, LFP exhibits lower energy density compared to alternatives such as NMC. Despite this limitation, LFP offers a distinct advantage: it retains structural integrity when nanosized. Nanosizing LFP particles yields several benefits, notably enhancing electrochemical performance in subzero environments. By reducing particle size, the surface area increases, improving reaction kinetics through shortened lithium-ion diffusion paths. This enables higher charge and discharge rates—an essential requirement for applications demanding high-power output under extreme cold conditions.

While active materials are critically important, the electrolyte plays a pivotal role in ensuring optimal battery performance at low temperatures.[8] It facilitates the transport of lithium ions between the anode and cathode, while simultaneously forming a solid-electrolyte interphase (SEI) layer that stabilizes electrode surfaces throughout the operational lifespan of LIBs.[9] Traditional low-concentration electrolytes often exhibit increased viscosity and reduced ionic conductivity under cold conditions, significantly impairing battery performance. The effectiveness of the electrolyte in such environments depends on precise control of its solvent and salt composition. The solvent must be optimized to ensure the electrolyte remains in a liquid state and retains low viscosity, even in extreme cold.

This study aimed to address the unique challenges faced by UASs operating under extreme conditions by developing a LIB with high-energy and high-power density, optimized for such environments. The project focuses on three key areas: the development of advanced anode and cathode materials, the formulation of low-temperature electrolytes, and the optimization of electrode architecture to enhance performance under the specific conditions encountered by UASs. For anodes, the

study explored the integration of Si into an HC matrix to leverage Si's high capacity while mitigating the adverse effects of its volume expansion. For cathodes, LFP was selected due to its excellent thermal stability, long cycle life, and favorable safety profile. Regarding electrolytes, the research centered on developing a localized high-concentration electrolyte (LHCE) capable of maintaining high ionic conductivity and stabilizing the SEI layer at low temperatures.[10] Careful selection and balancing of solvents and salts can yield an electrolyte with enhanced ionic conductivity, thereby improving ion transfer between electrodes and boosting the battery's overall power output.[8] This integrated approach—simultaneously optimizing active materials and electrolyte composition—may pave the way for energy storage solutions capable of meeting the rigorous demands of UASs in extreme environments.

2. Materials and Methods

2.1 Cell Assembly

For the cathode, LFP, along with polycrystalline (PC) or single-crystalline (SC) nickel cobalt manganese oxide (NCM) in a ratio of 60% nickel (Ni), 20% cobalt (Co), and 20% manganese (Mn) (NCM622), was selected as the active material. These were complemented by polyvinylidene fluoride (PVdF), Super-P (conductive carbon black), and single-walled carbon nanotubes (SWNTs). The components were mixed in a weight ratio of 80:10:9.5:0.5, cast onto aluminum (Al) foil, and dried in a vacuum oven at 120 °C for 8 h. The dried electrodes were then punched into disc shapes. For the anode, a composite of HC and Si was used in a specified weight ratio, combined with Dextran, Super-P, and SWNTs in a ratio of 80:9.8:10:0.2. This mixture was cast onto copper (Cu) foil and similarly dried at 120 °C for 8 h before being shaped into discs. CR2032 coin cells (Welcos) were assembled by stacking the cathode, 60 μL of electrolyte, a polyethylene (PE) separator, and the anode within the cell case.

2.2 Electrochemical Test

Electrochemical performance was evaluated using a battery cycler (WBCS 3000Le32, Wonatech). Anode half-cells were tested within a voltage range of 0.01 to 1.5 V, while cathode half-cells and full-cells were cycled between 1.8 and 4.2 V versus Li/Li^+. Electrochemical impedance spectroscopy (EIS) measurements were conducted over a frequency range of 1 to 100 MHz to assess internal resistance and charge-transfer characteristics.

3. Results and Discussion

3.1 Preliminary Studies of Cathodes, Anodes, and Electrolytes

To construct a battery system tailored for high discharge rate applications, modifications were made to the cathode, anode, and electrolyte components. The cathode was prioritized for initial optimization due to its critical role in facilitating lithium-ion migration during discharge. Achieving high-rate capability requires cathode materials with excellent kinetic properties and sufficient structural stability, especially under low-temperature operating conditions. Two active materials were selected for evaluation: LFP and NCM622. LFP, known for its robust polyanionic framework, offers tunable particle sizes ranging from nanometers to micrometers, enabling size-dependent performance testing. For NCM622, both PC and SC variants were investigated.

Figure 1a presents preliminary results indicating that, for all cathode active materials, the specific discharge capacity began to decline noticeably at a 2D discharge rate with a 0.5C charge rate in the half-cell configuration. A significant drop was observed at a 10D discharge rate. PC-NCM622 exhibited a higher specific discharge capacity than LFP. Figure 1b shows that PC-NCM622 demonstrated a significantly lower relative capacity compared to LFP in the full-cell configuration, particularly at a 10D discharge rate with a 1C charge rate. The relative capacity is defined as the measured capacity divided by the initial capacity. The results confirm that LFP is an optimal cathode active material for achieving higher power density.

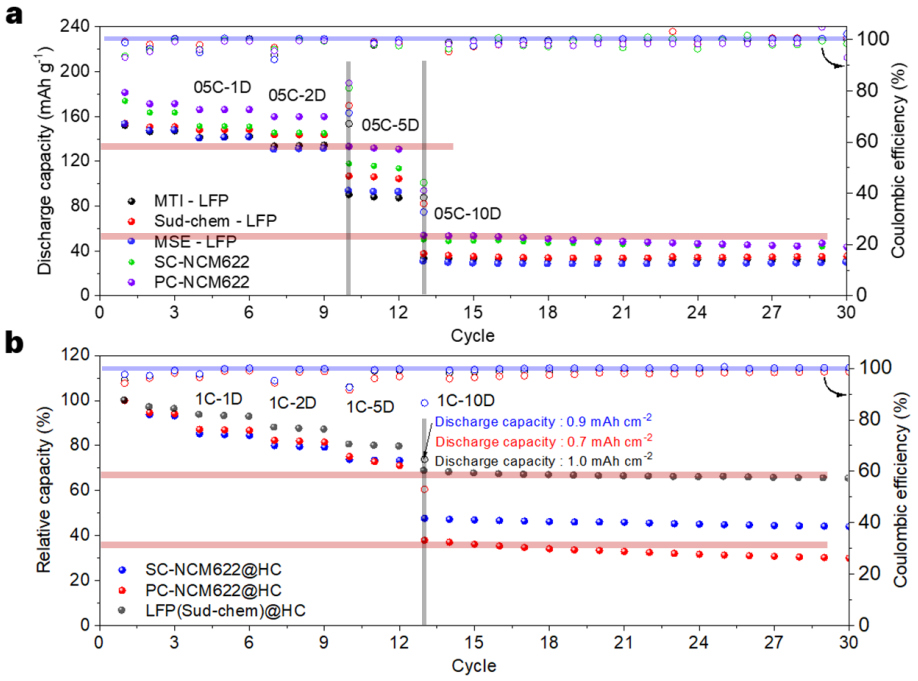

Figure 1. Evaluation of cathode active material in a) half-cell and b) full-cell with HC at room temperature.

Achieving the desired electrochemical performance for anodes requires determining the optimal ratio of active materials within the HC-Si composite. The Si content in the active material was selected at 7 wt%, 15 wt%, and 30 wt%. As shown in Figure 2, increasing the Si content led to an improvement in the initial coulombic efficiency (ICE) of the composite electrode; however, it also caused intensified volume expansion. The coulombic efficiency (CE) is defined as the discharge capacity divided by charge capacity. Discharge capacity is the total amount of electric charge a battery can deliver under specified conditions before it is fully discharged; it is measured in milliampere-hours (mAh). Charge capacity is the total amount of electric charge a battery can accept during the charging process, and is also measured in mAh.

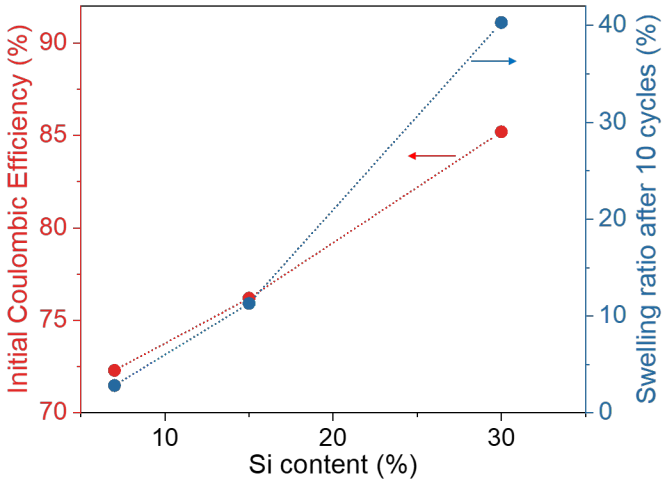

Figure 2. ICE (left, red) and swelling after 10 cycles (right, blue) vs. Si content.

Figure 3 illustrates electrode swelling observed in a half-cell configuration using scanning electron microscopy (SEM). Two electrolyte formulations were evaluated in comparison to the pristine electrode: one composed of lithium bis(fluorosulfonyl)imide (LiFSI), 1,2-dimethoxyethane (DME), and 1,1,2,2-tetrafluoroethyl-2,2,3,3-tetrafluoropropyl ether (TTE) in a molar ratio of 1:2.7:3 (LiFSI-DME-TTE); and another composed of LiFSI, DME, fluoroethylene carbonate (FEC), and TTE in a molar ratio of 1:2:1:3 (LiFSI-DME-FEC-TTE). These formulations were selected to examine the impact of fluorinated additives and solvent ratios on electrode stability and interfacial behavior. The inclusion of FEC is intended to suppress Si-induced volume expansion and improve battery cell performance. Note that the initial thicknesses of the pristine electrodes are different. As shown in Figure 4, increasing the Si content leads to exponential volume expansion, while the addition of FEC reduces this expansion by more than 60%.

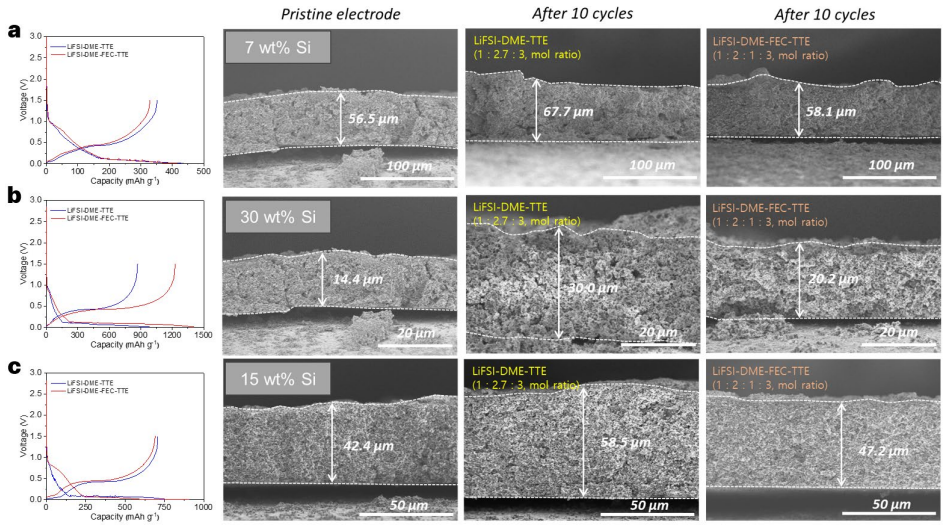

Figure 3. Voltage profile of half-cell and volume expansion in cross-sectional SEM image of a) 7 wt% Si, b) 30 wt% Si, and c) 15 wt% Si.

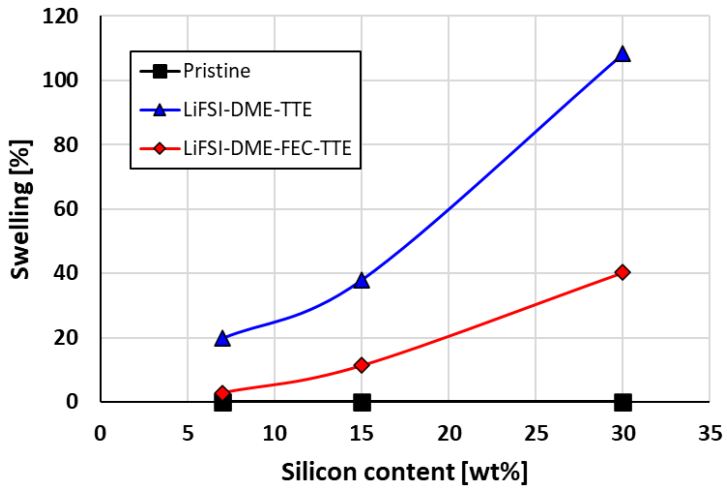

Figure 4. Swelling with respect to Si content for pristine and two different electrolyte electrodes.

To assess the compatibility of the composite anode material with the cathode, a full-cell was fabricated and evaluated using the previously selected nanosized LFP as the cathode. The results show that battery cells containing 15 wt% and 30 wt% Si exhibited higher battery cell capacity, as shown in Figure 5 (left column), while the 7 wt% sample demonstrated higher discharge rate capability, as shown in Figure 5 (right column). Battery cell capacity is defined as the total amount of electrical charge a single battery cell can store and deliver. It indicates how long a battery-powered device can operate before needing a recharge.

Considering the battery cell ICE and Si volume expansion across different Si contents in both half-cell and full-cell configurations, 15 wt% was selected as the optimal content. The 7 wt% exhibited lower ICE, while the 30 wt% showed significant volume expansion in the anode.

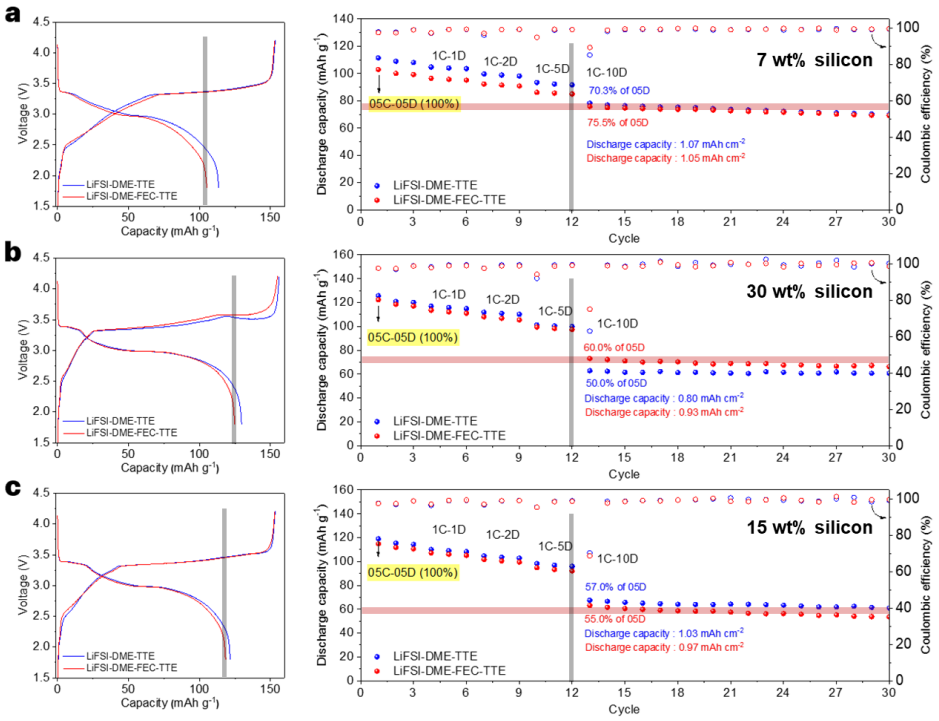

Figure 5. Voltage profile of full-cell in formation cycle and rate capability test at a) 7 wt% Si, b) 30 wt% Si, and c) 15 wt% Si.

3.2 Electrolyte Evaluation

Designing the electrolyte aimed to maximize the discharge rate at low temperatures using the selected anode and cathode materials. Solvents capable of maintaining low viscosity under extreme cold conditions were considered. The conceptual analysis showed that DME and butyl methyl ether (BME), from the ether group, are the most promising candidates (see Figure 6a).

DME acts as a strong solvent as it interacts with salts. However, BME is relatively weaker due to its longer hydrocarbon chain. An LHCE was designed to optimize the solvation structure for effective operation at both low and room temperatures. TTE is one of the most commonly used diluents in such formulations. Several critical factors in efficient lithium-ion transport include liquid-phase diffusion within the bulk electrolyte, the de-solvation process at the electrode–electrolyte interface, the resistivity of the interfacial layer, and the charge-transfer resistance within each active material. Figure 6b illustrates the conceptual processes described above.

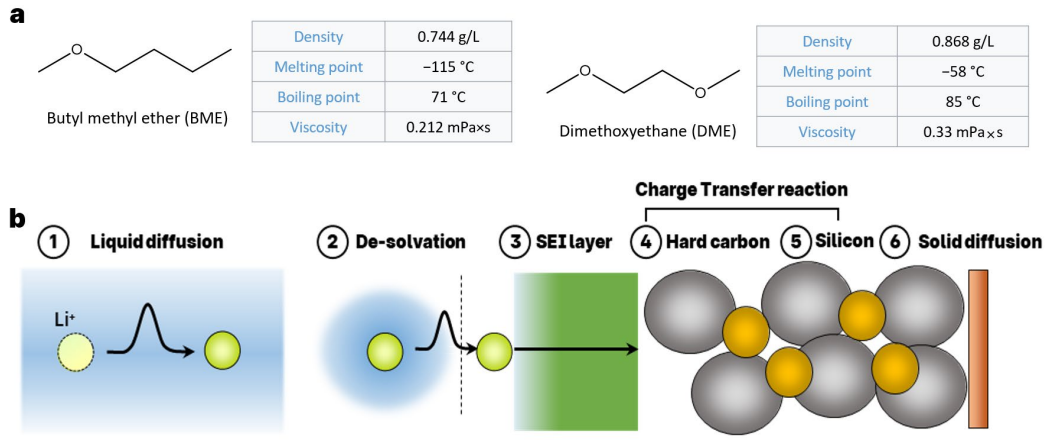

Figure 6. a) Candidate solvents within the ether group and b) the influence of multiple factors on LIB operation.

Figure 7 shows comprehensive cell evaluation results for the LHCE using DME and BME as single solvents and in combination. Figure 7a presents no significant differences in battery cell capacity or in the charge and discharge voltage profiles at 25 °C (i.e., room temperature). Figure 7b shows that LiFSI-DME-BME-TTE outperformed at high discharge rates at room temperature. Specific discharge capacity at –20 °C drastically decreased under all test conditions and significantly declined with increasing discharge rate, even at a 0.5C charge rate (see Figure 7c). LiFSI-DME-BME-TTE performed better at higher discharge rates at –20 °C, but its specific discharge capacity was less than 20 mAh/g. In Figure 7d, LiFSI-DME-BME-TTE showed higher relative capacity at higher discharge rates at room temperature, while it exhibited lower relative capacity at a 1D discharge rate. LiFSI-BME-FEC-TTE underperformed under all test conditions.

Notably, the LHCE formulated with both solvents (i.e., DME and BME) yielded the most favorable results at high discharge rates and under extreme cold temperatures, compared to those containing either solvent alone. Strong solvents such as DME offer excellent ionic conductivity within the bulk electrolyte, while weaker solvents like BME provide advantages in de-solvation at the electrode interface. When combined, the activation energies associated with each solvent are reduced, resulting in a synergistic effect that enhances overall electrochemical performance.

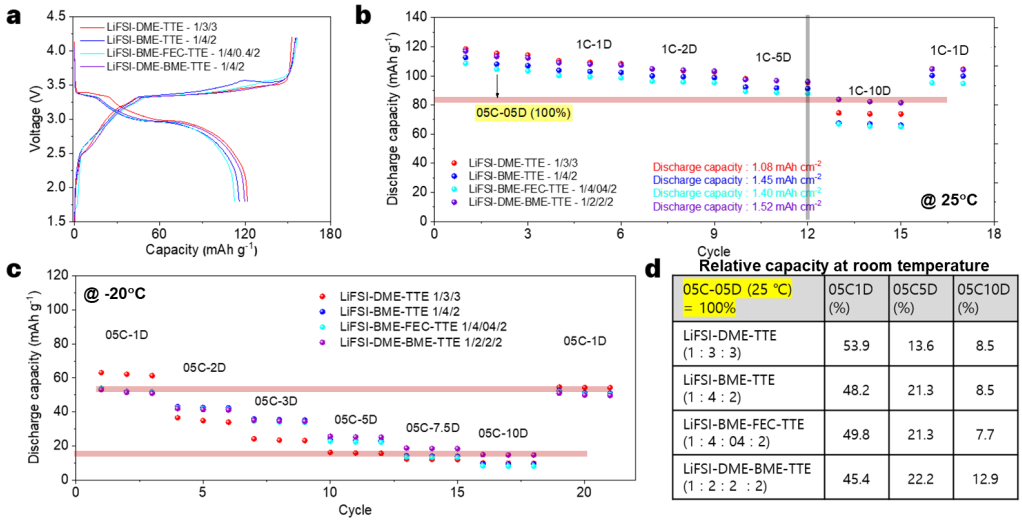

05C-05D (25 ℃) = 100%	05C1D (%)	05C5D (%)	05C10D (%)
LiFSI-DME-TTE (1 : 3 : 3)	53.9	13.6	8.5
LiFSI-BME-TTE (1 : 4 : 2)	48.2	21.3	8.5
LiFSI-BME-FEC-TTE (1 : 4 : 04 : 2)	49.8	21.3	7.7
LiFSI-DME-BME-TTE (1 : 2 : 2 : 2)	45.4	22.2	12.9

Figure 7. Evaluation of electrolytes in full-cell: a) formation cycle, b) rate capability test in room temperature, c) rate capability test in –20 °C, and d) relative capacity compared at room temperature.

3.3 Optimization for Low-Temperature Operation

The discharge rate at –20 °C still needs improvement; thus, further optimization of the electrolyte was performed. Figure 8a shows the chemical structures of the solvents, additive, and diluent assessed above. In the solvation clusters, the stronger solvent dominates at room temperature, while the weaker solvent becomes more influential at low temperature (see Figure 8b). This dynamic leads to the formation of a stable solvation structure that prevents salt precipitation across a wide range of temperatures. Accordingly, the spatial distribution of these solvation clusters, shown in Figure 8c, significantly affects the rate characteristics of the cell. Conventional LHCE (C-LHCE) exhibits suboptimal performance at low temperatures, primarily due to the excessive use of diluent and the resulting lack of connectivity between solvation clusters. In contrast, the medium LHCE (M-LHCE) achieves optimal performance under low-temperature conditions by reducing the diluent content, increasing the proportion of solvent, and maintaining low viscosity. This formulation ensures effective connectivity between solvation clusters, thereby enhancing overall electrochemical performance.

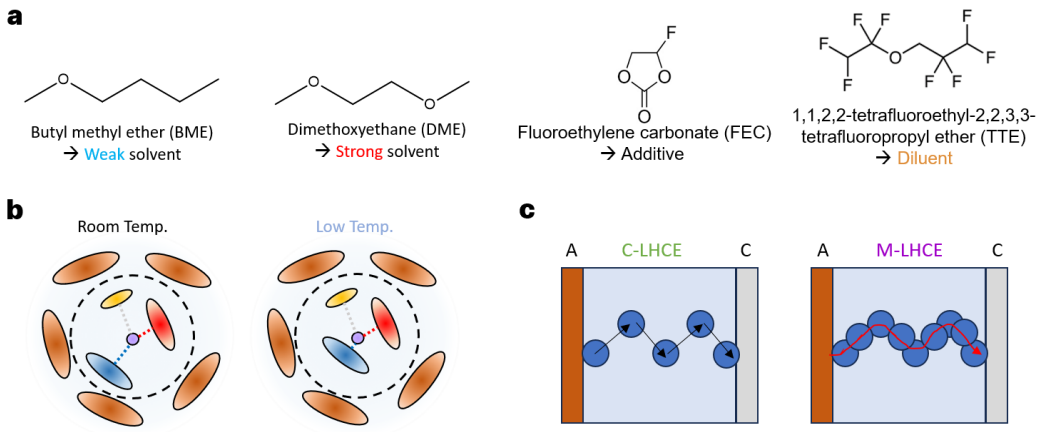

Figure 8. a) Each component of the electrolyte, b) difference of interaction in solvation cluster at room and low temperature, and c) forming bridges of solvation cluster in C-LHCE and M-LHCE.

A comparative evaluation was conducted by adjusting the solvent and diluent composition within the LHCE. Specifically, the salt–solvent–diluent molar ratio was set to 1:4:2 for the C-LHCE and 1:6:1 for the M-LHCE. In addition, FEC was added to enhance low-temperature characteristics. In Figure 9a, the battery cell capacity slightly decreased with increasing solvent and decreasing diluent. Figure 9b shows no significant differences in discharge capacity at the 10D discharge rate and room temperature, while an increase in diluent reduced the discharge capacity at lower discharge rates. However, the specific discharge capacity significantly increased with the higher solvent content and the addition of FEC at –20 °C (see Figure 9c). Still, the discharge capacity at high discharge rates remains low, measuring approximately 25 mAh/g at the 10D discharge rate. In Figure 9d, M-LHCE showed a 1.6× higher relative capacity at the 1D discharge rate and a 1.8× increase at the 10D discharge rate at room temperature. The relative improvement is attributed to the addition of FEC, which leads to the formation of a supplementary lithium-fluoride layer. This results not only in the suppression of Si volume expansion but also in the reduction of interfacial resistance at low temperatures. Nevertheless, the relative capacity remains low (23.2%) at the 10D discharge rate for M-LHCE.

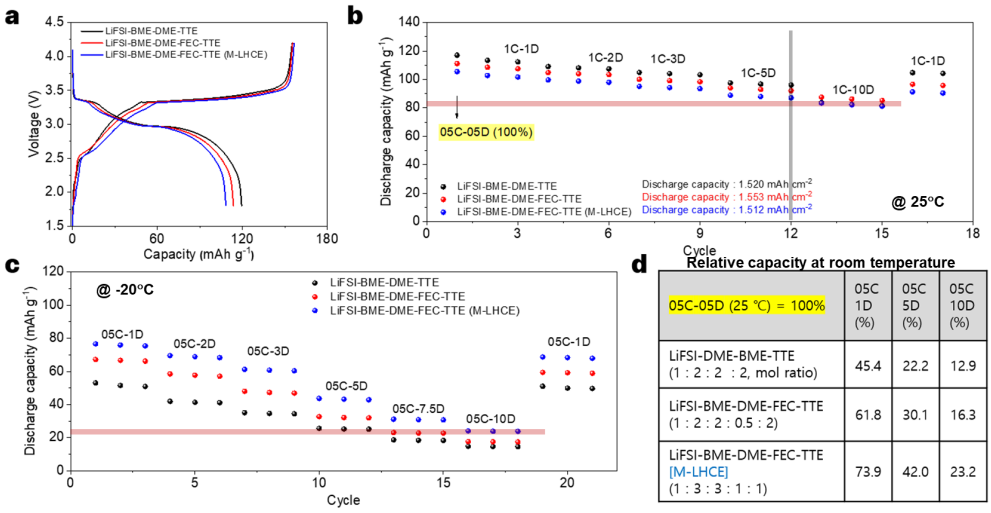

05C-05D (25 ℃) = 100%	05C 1D (%)	05C 5D (%)	05C 10D (%)
LiFSI-DME-BME-TTE (1 : 2 : 2 : 2, mol ratio)	45.4	22.2	12.9
LiFSI-BME-DME-FEC-TTE (1 : 2 : 2 : 0.5 : 2)	61.8	30.1	16.3
LiFSI-BME-DME-FEC-TTE [M-LHCE] (1 : 3 : 3 : 1 : 1)	73.9	42.0	23.2

Figure 9. Evaluation with adjusting ratio in electrolyte: a) formation cycle, b) rate capability test in room temperature, c) rate capability test in –20 °C, and d) relative capacity compared at room temperature.

EIS analysis was performed over a range of frequencies at room temperature to assess the resistance behavior of battery cells containing three different electrolytes. Distribution relaxation time (DRT) analysis was subsequently conducted to more clearly present the distinct electrochemical processes through a distribution of time constants, which reveals the number of processes present and their behavior over time. Figure 10a presents the imaginary part of impedance on the y-axis and the real part on the x-axis. The results show that the electrolyte without FEC exhibited higher electrolyte resistance. In contrast, the electrolytes containing FEC displayed higher charge-transfer resistance and increased lithium-ion diffusion resistance. In Figure 10b, the DRT results reflected the same trends but revealed more detailed electrochemical processes than the Nyquist plot.

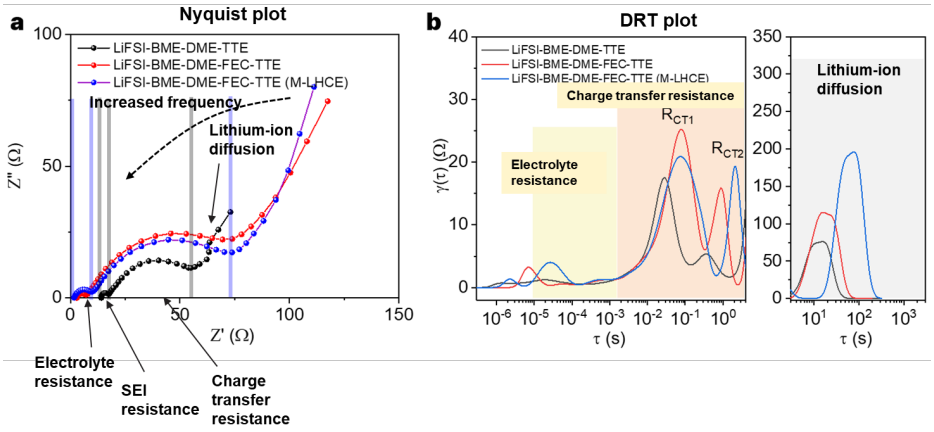

Figure 10. a) EIS spectra and b) DRT convert of adjusting ratio in electrolyte test.

After determining the active materials and electrolyte, the electrode architecture was optimized to enable high discharge performance at low temperatures. Low-loading electrode coatings and mesh electrode structures were assessed for their potential benefits in achieving fast charge–discharge cycles and stable operation under low-temperature conditions. Optimized electrolyte performance was also compared against that of a pure HC anode. Figure 11 shows that the pure HC anode exhibited significantly lower battery cell capacity and specific discharge capacity under all test conditions. Figure 11b indicates no significant differences in specific discharge capacity among the different loadings and structures at room temperature. However, the low loading with the mesh structure demonstrated a higher specific discharge capacity at –25 °C, reaching nearly 40 mAh/g, as shown in Figure 11c. Relative capacity at room temperature further confirmed that the low loading with the mesh structure performed better than the other configurations (see Figure 11d).

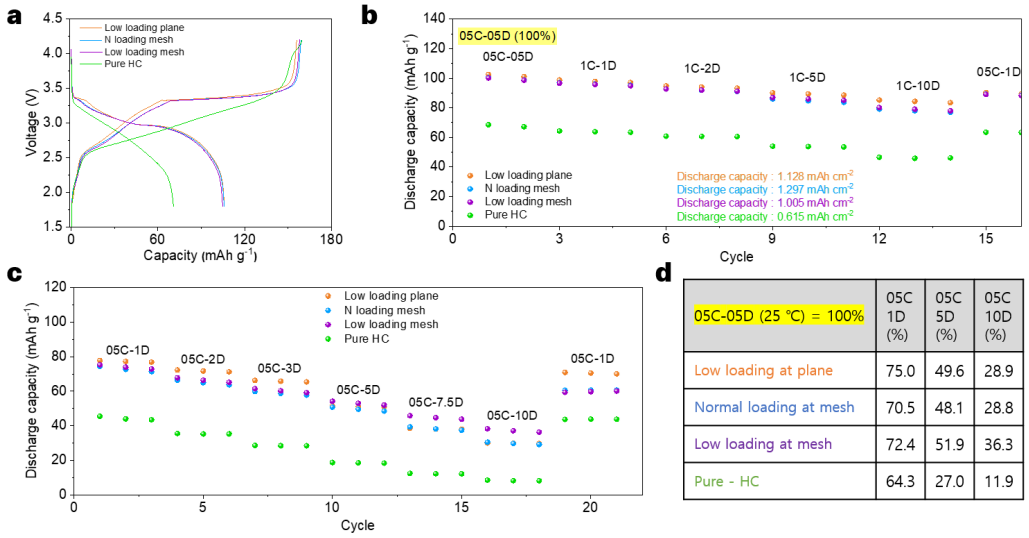

05C-05D (25 °C) = 100%	05C 1D (%)	05C 5D (%)	05C 10D (%)
Low loading at plane	75.0	49.6	28.9
Normal loading at mesh	70.5	48.1	28.8
Low loading at mesh	72.4	51.9	36.3
Pure - HC	64.3	27.0	11.9

Figure 11. Evaluation with low-loading plane electrode or mesh electrode: a) formation cycle, b) rate capability test in room temperature, c) rate capability test in –20 °C, and d) relative capacity compared at room temperature.

In Figure 12a, the EIS analysis shows that coating the electrode surface over a mesh structure led to reduced electrolyte resistance compared to the planar electrode, which may be attributed to the increased surface area. Aside from this, no major differences were observed in the remaining resistance components among the different architectures in this experiment. In Figure 12b, the Nyquist and DRT analyses results indicate that the pure HC exhibited extremely high charge-transfer resistance, which is attributed to its poor performance at –20 °C.

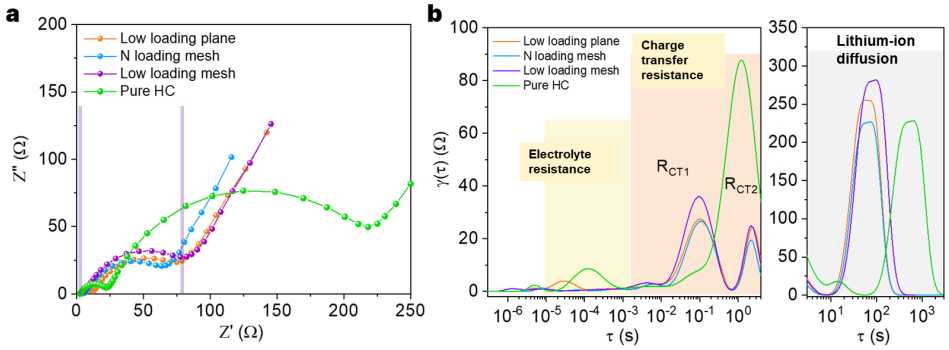

Figure 12. a) EIS spectra and b) DRT convert of electrode architecture test.

3.4 Silicon Content Optimization

A preliminary assessment of Si content on battery cell performance is presented in Section 3.1. This section further explores the optimization of Si content within the designed electrolyte. All electrochemical characterization was performed using full-cell configurations. Figure 13 shows that higher Si content clearly increased both battery cell capacity and specific discharge capacity, particularly at room temperature. In Figure 13b, the specific discharge capacity gradually decreased with increasing discharge rate at room temperature. At –20 °C (see Figure 13c), the rate of decrease became more pronounced. Higher Si content exhibited greater specific discharge capacity at discharge rates of 3D and below, while specific discharge capacities were relatively insensitive to Si content at discharge rates above 5D. Figure 13d shows that Si contents of 7 wt% and 15 wt% resulted in higher relative capacity compared to both pure HC and 30 wt% Si content.

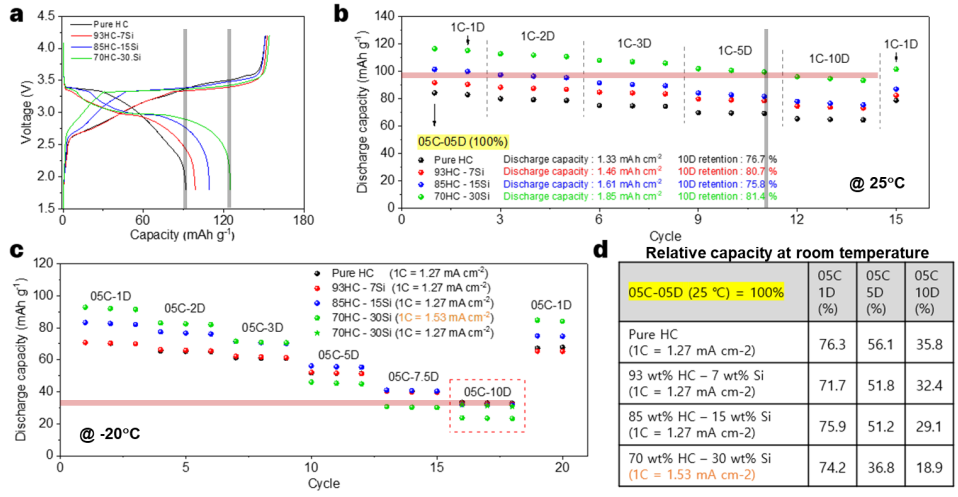

05C-05D (25 °C) = 100%	05C 1D (%)	05C 5D (%)	05C 10D (%)
Pure HC (1C = 1.27 mA cm-2)	76.3	56.1	35.8
93 wt% HC – 7 wt% Si (1C = 1.27 mA cm-2)	71.7	51.8	32.4
85 wt% HC – 15 wt% Si (1C = 1.27 mA cm-2)	75.9	51.2	29.1
70 wt% HC – 30 wt% Si (1C = 1.53 mA cm-2)	74.2	36.8	18.9

Figure 13. Evaluation by adjusting Si ratio in anode at low temperature: a) formation cycle, b) rate capability test in room temperature, c) rate capability test in –20 °C, and d) relative capacity compared at low temperature.

Figure 14 presents the EIS and DRT analyses for battery cells with three different Si contents and a pure HC anode. The EIS results in Figure 14a show no significant variations among the different anode materials at room temperature. However, the DRT analysis in Figure 14b reveals that higher Si content corresponds to longer relaxation times, while lower Si content and HC exhibit bimodal charge-transfer resistance behavior. Unlike the results at room temperature, the Nyquist plot in Figure 14c displays abnormal behavior and significantly increased resistance. The DRT analysis at –20 °C, shown in Figure 14d, indicates that charge-transfer resistance shifts to longer relaxation times and increases drastically across all anode materials. Among the tested Si contents, the 15 wt% composition exhibited the lowest overall resistance under extreme temperature conditions.

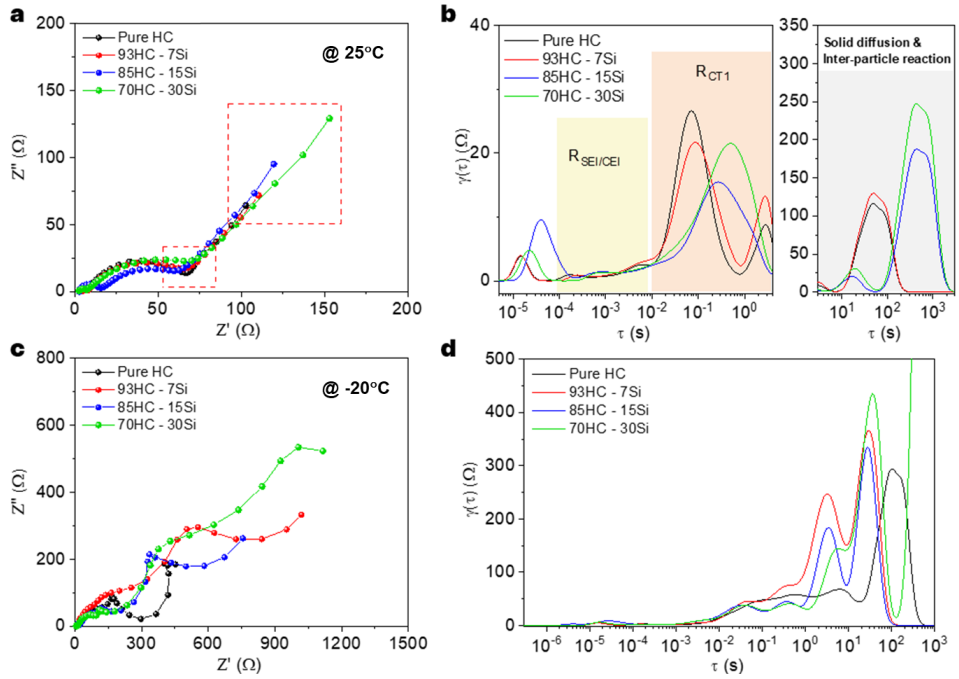

Figure 14. a) EIS spectra and b) DRT convert of adjusting Si ratio at room temperature. c) EIS spectra and d) DRT convert of adjusting Si ratio at –20 °C.

Further electrolyte optimization was performed using Si contents of 15 wt% and 30 wt%. Figure 15a shows instability in the 30 wt% Si electrode during the charging phase of the formation cycle. As shown in Figure 15b, the specific discharge capacity exhibited minimal sensitivity to both Si content and electrolyte composition at room temperature. However, at –20 °C, the 30 wt% Si electrode demonstrated poor stability in DME-rich electrolytes, while the 15 wt% Si electrode paired with a BME-dominant electrolyte showed the most favorable performance (see Figure 15c). The relative capacity results in Figure 15d indicate that the 15 wt% Si electrode with the BME-dominant electrolyte exhibited the highest relative capacity across all discharge rate conditions.

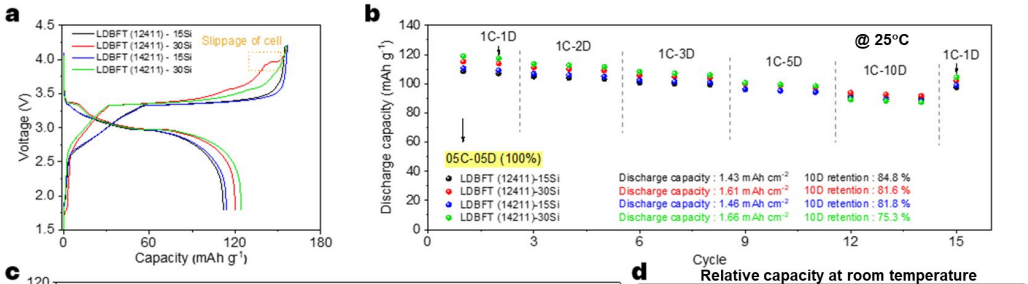

05C-05D (25 °C) = 100%	05C1 D (%)	05C5 D (%)	05C10 D (%)
LDBFT(12411) - 15 wt% Si (1C = 1.27 mA cm-2)	77.0	51.5	26.4
LDBFT(12411) - 30 wt% Si (1C = 1.27 mA cm-2)	75.2	43.7	20.4
LDBFT(14211) - 15 wt% Si (1C = 1.27 mA cm-2)	76.0	42.0	22.7
LDBFT(14211) - 30 wt% Si (1C = 1.27 mA cm-2)	54.6	31.0	18.9
LDBFT(13311) - 15 wt% Si (1C = 1.27 mA cm-2)	75.9	51.2	29.1

Figure 15. Evaluation by adjusting electrolyte ratio at low temperature: a) formation cycle, b) rate capability test in room temperature, c) rate capability test in –20 °C, and d) relative capacity compared at low temperature.

In Figures 16a and 16b, the EIS and DRT analyses results show that higher Si content reduced charge-transfer resistance at room temperature; however, lithium-ion diffusion resistance increased with increasing Si content. In contrast, at –20 °C, both EIS and DRT analyses reveal that higher Si content significantly increased charge-transfer resistance and shifted it to longer relaxation times (see Figures 16c and 16d). The 15 wt% Si content electrode with the BME-rich electrolyte exhibited slightly lower total resistance. These results suggest compromised electrode–electrolyte compatibility under extreme cold conditions.

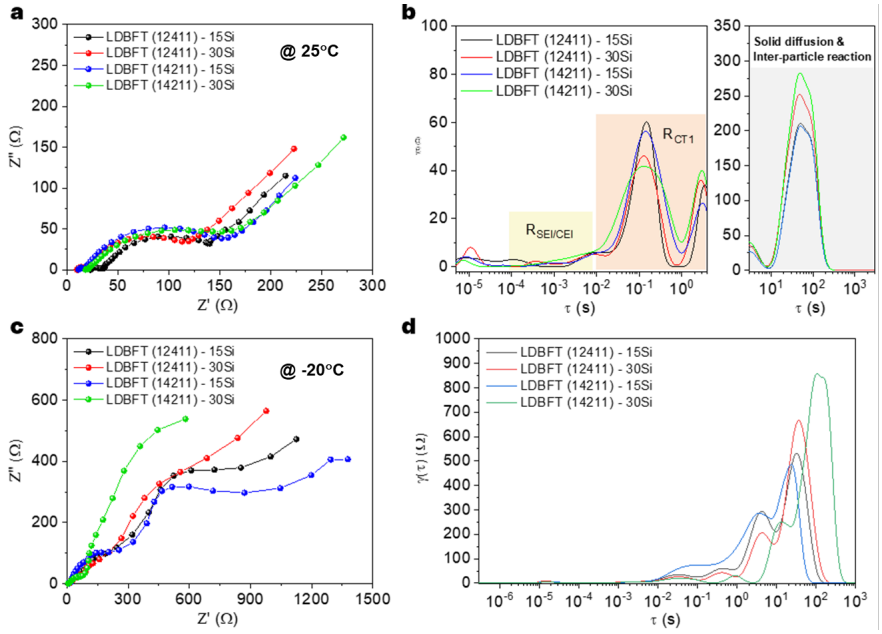

Figure 16. a) EIS spectra and b) DRT convert of adjusting electrolyte ratio at room temperature. c) EIS spectra and d) DRT convert of adjusting electrolyte ratio at –20 °C.

Si content optimization revealed that higher Si content consistently increased both the specific discharge capacity and the ICE across all tested electrolytes (see Figure 17a). Discharge rate testing was conducted at 10D at room temperature and 5D at –20 °C. Figure 17b shows that retention at 10D increased with rising Si content and reached an asymptote at 15 wt% when using an electrolyte with equal amounts of DME and BME at room temperature. The use of a BME-dominant electrolyte improved 10D retention at 15 wt% but led to a rapid decline at higher Si contents. In contrast, the DME-dominant electrolyte did not enhance 10D retention at 15 wt% and accelerated the decline as Si content increased.

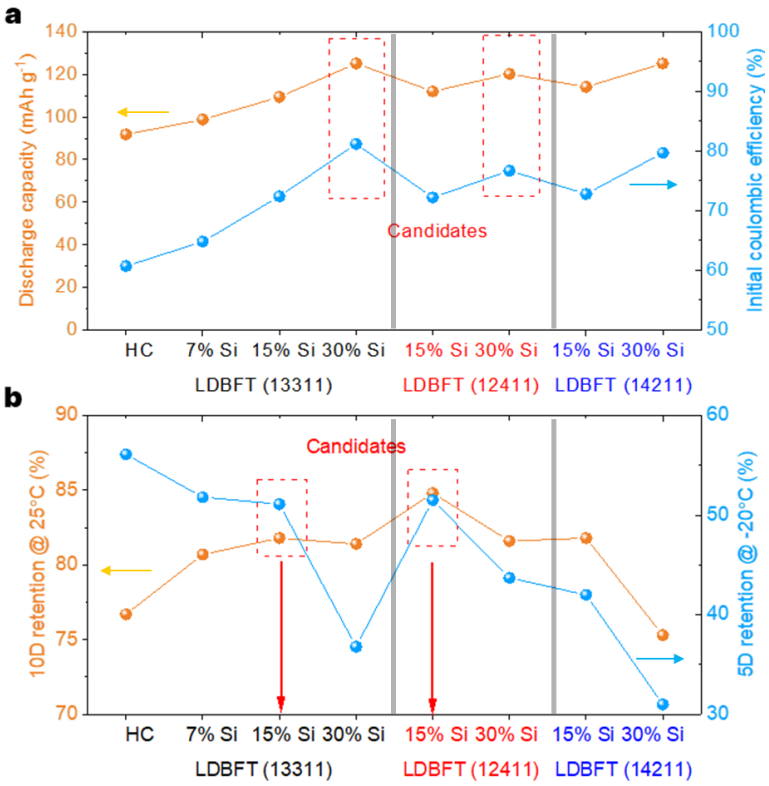

Figure 17. Optimization plot for Si ratio and electrolyte ratio in a) formation cycle and b) rate cycle at room temperature and –20 °C.

At –20 °C, the electrolyte with equal amounts of DME and BME showed a gradual decrease in 5D retention with increasing Si content, followed by a sharp drop beyond 15 wt%. The BME-dominant electrolyte maintained consistent 5D retention at 15 wt%, but then declined rapidly with further increases in Si content. The DME-dominant electrolyte reduced 5D retention even at 15 wt% and further accelerated the decline at higher Si levels.

These results indicate that while higher Si content enhances specific discharge capacity and ICE, there is an optimal Si content for achieving better performance at high discharge rates and under extreme cold conditions. The study identified 15

wt% as the optimal Si content, with preferred electrolyte compositions being LiFSI-DME-BME-FEC-TTE (LDBFT) with a molar ratio of 1:3:3:1:1 (13311) and LDBFT (12411). Among these, LDBFT (13311) demonstrated slightly better performance than LDBFT (12411).

Compared to the state-of-the-art electrolyte compositions published in major journals,[11–14] LDBFT (13311) exhibited comparable ionic conductivity, except for one formulation (i.e., formulation 11; see Figure 18a). Although LDBFT (13311) showed a slightly lower overall cell capacity, its low-temperature discharge current density is significantly higher than those of the state-of-the-art electrolyte compositions (see Figure 18b).

a

ref #	Journel	Electrolyte composition	Ionic conductivity (mS cm^{-1})
-	This work	(LiFSI-BME-DME-FEC-TTE) (1 : 3 : 3 : 1 : 1, mol ratio) – 1.10 M	25 °C : 8.0 -20 °C : ~ 2.5
11	Nature	1.3 M LiFSI in FAN (fluoroacetonitrile)	25 °C : 40.0 -20 °C : ~ 20.0
12	Nature	1.0M LiTFSI in MDFA:MDFSA:TTE = 4:1:5, volume ratio	25 °C : 4.0 -20 °C : ~ 2.0
13	Nat. Energy	1 M $LiPF_6$ in PC:FEC: TFEA (ethyl 2,2,2-trifluoroethyl carbonate) (8:1:1, v/v/v) with 10 wt% tris(pentafluorophenyl) borane, 5 wt% $LiBF_4$, and 0.5 wt% $LiNO_3$	25 °C : 6.0 ~ 8.0 -20 °C : ? (Paper was not focused on EL)
14	Nat. Commun.	2.0 M LiFSI in BFE (bis(2-fluoroethyl) ethers)	25 °C : 9.0 -20 °C : 3.0

b

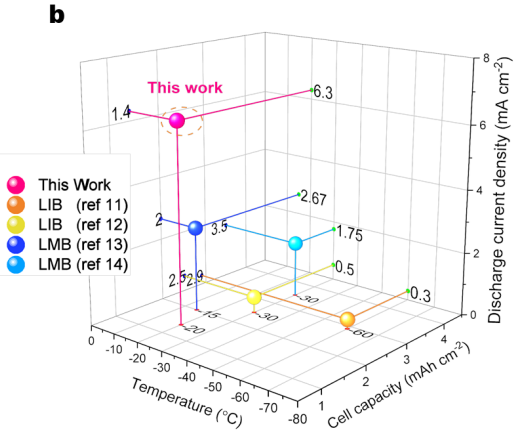

Figure 18. a) Comparison table and b) performance plot with other state-of-the-art papers.

3.5 Long-Term Performance Improvement

Battery cell long-term cycling stability is critical in real-world applications, as it directly impacts operation and sustainment costs. Figures 19a and 19b show the specific discharge capacity at room temperature and at –20 °C, respectively, with respect to the number of cycles. Long-term cycling tests were performed at 3D and 10D discharge rates at room temperature, and at a 5D discharge rate at –20 °C. Reliable cycle stability at discharge rates higher than 10D at room temperature and 5D at –20 °C was not achievable.

In Figure 19a, the HC battery cell at 1C charge and 3D discharge rates exhibited stable long-term cycling and capacity retention, although its specific discharge rate was lower than that of the Si-anode battery cells. The Si-anode battery cells showed faster degradation with cycling. Battery cell degradation, or cycling stability, rapidly decreased with increasing discharge rates at room temperature (see Figure 19a) or during low-temperature operation (see Figure 19b).

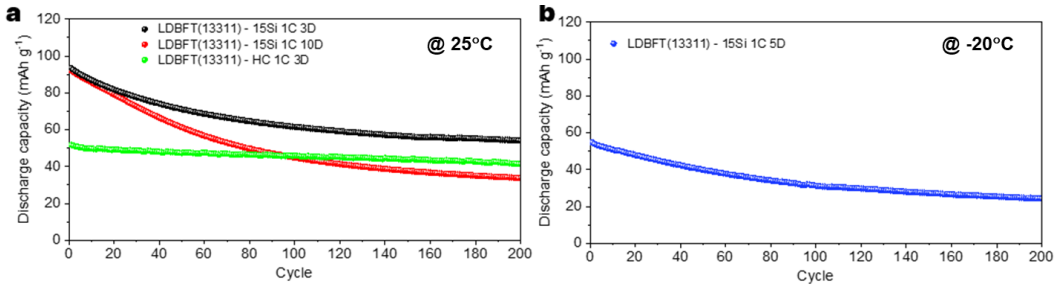

Figure 19. Long-term cycle performance at a) room temperature and b) –20 °C.

To address this issue, electrolyte additives and binder modifications were investigated. Figure 20c shows that the addition of 5 wt% vinylene carbonate (VC) improved long-term cycling stability at room temperature. However, cross-linking poly(acrylic acid) (PAA) with dextran was ineffective in enhancing cycling stability. Short-term cycling stability was not noticeably affected by the addition of VC. Figure 20a illustrates differences in charging behaviors between dextran and dextran-PAA, with dextran-PAA exhibiting a higher voltage increase at the beginning of charging. These results suggest that mechanical failure caused by rapid volume expansion during charging may influence degradation pathways. One suggested strategy is to reduce charge rates and increase discharge rates to mitigate mechanical stress during charging.

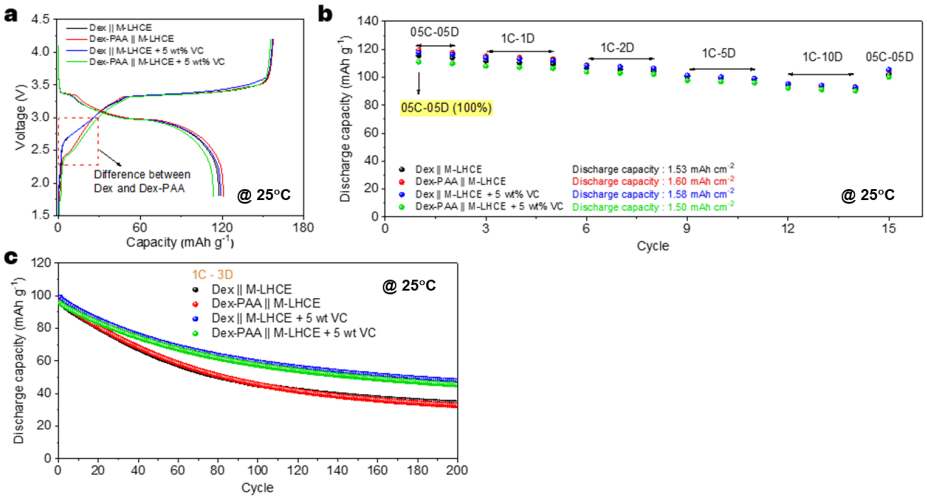

Figure 20. Evaluation with additives and cross-linked binder at room temperature: a) formation cycle, b) rate capability test at room temperature, and c) long-term cycle performance.

To improve the long-term cycling stability of Si-anode battery cells, Chemical Vapor Deposition silicon (CVD-Si) was deposited onto the surface of porous HC using a CVD method. Two types of electrodes were investigated: 1) electrodes composed solely of CVD-Si as the active material; and 2) composite electrodes containing both HC and CVD-Si, adjusted to achieve a specific capacity of

approximately 700 mAh/g (equivalent to ~15 wt% Si content). Figure 21 presents voltage profiles during charging and discharging relative to battery-cell–specific capacity (Figure 21a), alongside the specific discharge capacity as a function of cycle number for the two electrodes and a conventional 15% Si-based electrode. In Figure 21a, all three electrodes exhibited similar discharge capacities and ICE (estimated by comparing charge and discharge capacities). However, as the discharge rate increased, their behaviors diverged (see Figure 21b). The pure CVD-Si electrodes showed unstable behavior even at a 1D discharge rate, likely due to insufficient kinetic properties. In contrast, the composite CVD-Si electrode demonstrated rate performance slightly lower than that of the reference 15% Si electrode, confirming the effectiveness of balancing kinetics and stability.

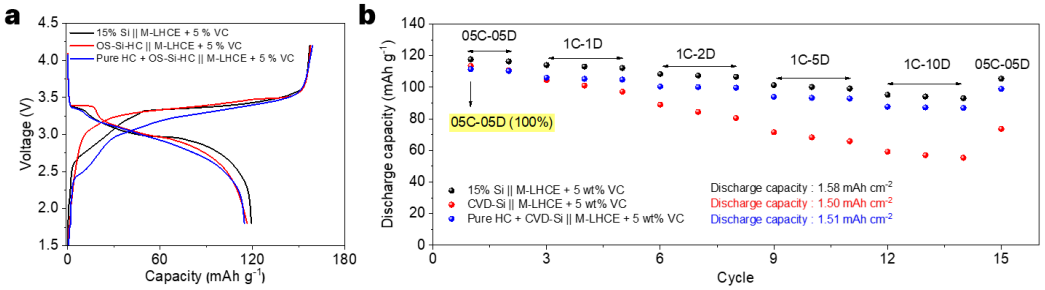

Figure 21. Evaluation with CVD-Si–based anode: a) formation cycle and b) rate capability test in room temperature.

Figure 22 presents the potential of CVD-Si active materials for improved long-term cycling at room temperature. In Figure 22b, the pure CVD-Si electrode outperformed the reference 15% Si electrode at 1C charge and 3D discharge rates. The composite CVD-Si electrode exhibited more stable cycling performance even without the VC additive. At 5D and 10D discharge rates (shown in Figures 22c and 22d, respectively), the CVD-Si electrodes maintained improved cycling stability with and without the VC additive. After 200 cycles, capacity retention remained near 82% and 69% at 5D and 10D discharge rates, respectively. These results demonstrate that CVD-Si better endures rapid volume expansion and sustains stable electrochemical performance. However, capacity retention decreased by over 22% for the composite CVD-Si with the VC additive at a 10D discharge rate at room temperature after 200 cycles. The specific discharge capacity did not change significantly at discharge rates of 5D and below at room temperature.

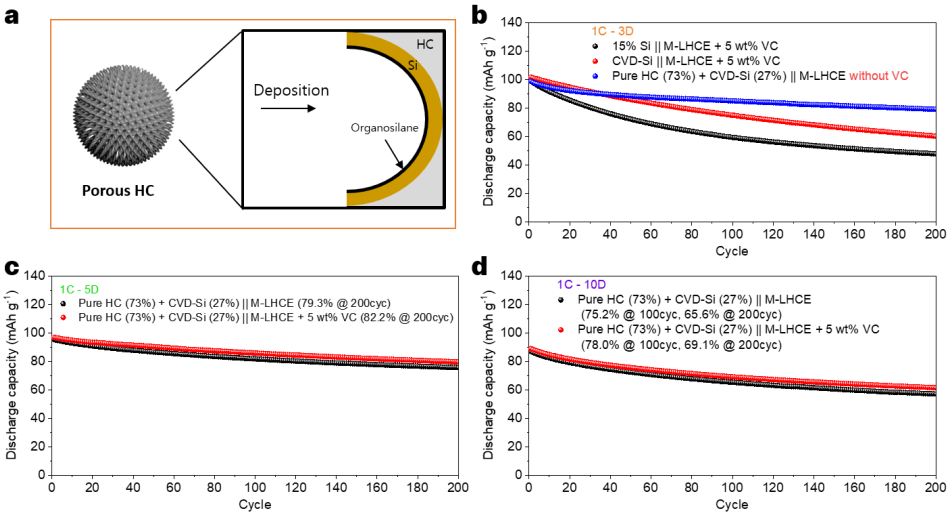

Figure 22. a) Schematic illustration of the surface of CVD-Si. Long-term cycle performance of b) 1C-3D, c) 1C-5D, and d) 1C-10D operation at room temperature.

Low-temperature performance evaluations were conducted at 0 and –20 °C to assess the rate capability and durability of CVD-Si electrodes. Figure 23a shows that the CVD-Si electrode performed slightly better than the reference 15% Si electrode across all discharge rates, while maintaining relatively stable cycling behavior at 0 °C. The specific discharge capacity declined by approximately 24% at 10D compared to the 1D discharge rate. At –20 °C, as shown in Figure 23b, the specific discharge capacity decreased by approximately 37% at a 5D discharge rate and declined nearly 65% at a 10D discharge rate. At discharge rates higher than 2D, the reference 15% Si electrode outperformed the CVD-Si electrode with the VC additive. However, the recovery capacity at a 1D discharge rate was higher for the CVD-Si electrode than for the reference 15% Si electrode.

Long-term cycling stability at low temperatures was further assessed for the CVD-Si electrode in comparison to the reference 15% Si electrode. Figure 24 shows the specific discharge capacity as a function of cycle number for both electrodes at 0 °C (Figure 24a) and –20 °C (Figure 24b). The experiment was conducted at 0.5C charge and 5D discharge rates. At –20 °C, a 3D discharge experiment was also performed to evaluate the effect of discharge rate on capacity retention. At 0 °C and 5D discharge rate, the CVD-Si electrode performed slightly better than the reference 15% Si electrode. At –20 °C and the same 5D discharge rate, the CVD-Si electrode outperformed the reference electrode in discharge capacity, maintaining over 90% capacity retention after 200 cycles. However, the CVD-Si electrode initially exhibited a lower specific discharge capacity than the reference electrode. When the discharge rate was decreased from 5D to 3D, the CVD-Si electrode displayed typical cycling behavior.

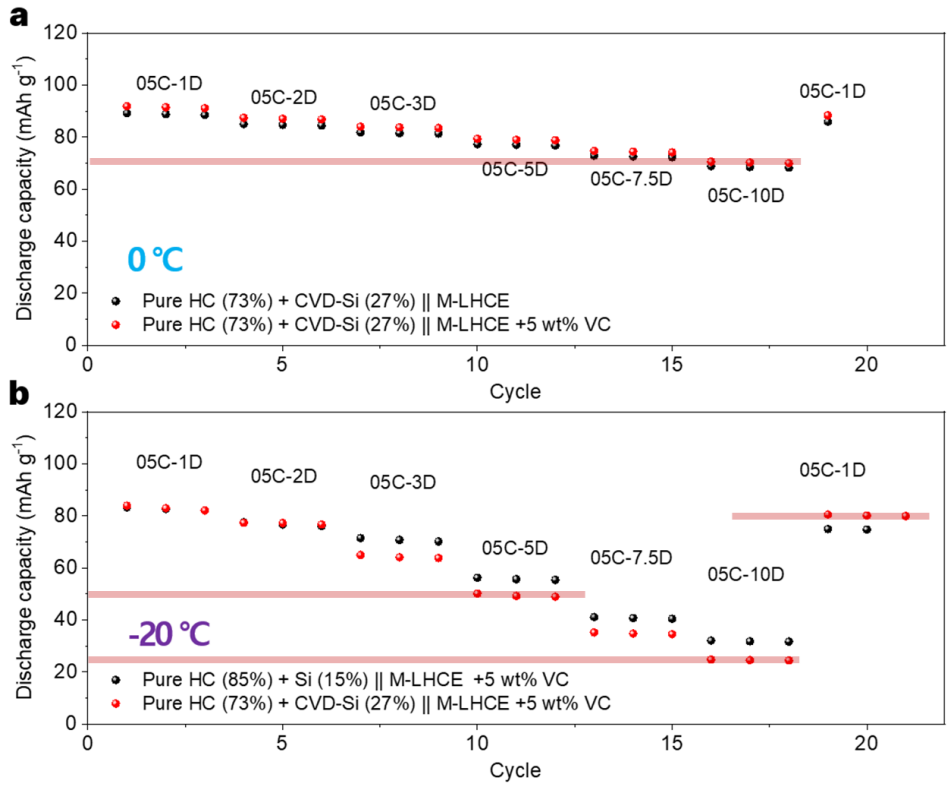

Figure 23. Rate capability test in low-temperature conditions at a) 0 ℃ and b) –20 ℃.

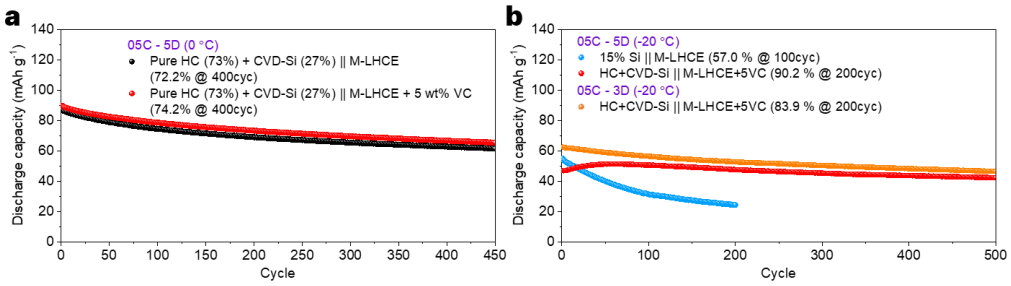

Figure 24. Long-term cycle performance in low-temperature conditions at a) 0 ℃ and b) –20 ℃.

3.6 Scalability Validation

The scalability of the CVD-Si electrode was assessed by reproducing it in a pouch cell format. The coin cell has an electrode area of approximately 0.785–1.1304 cm², while the pouch cell has a minimum area of 12 cm², based on the cathode. A larger electrode area may reveal current inhomogeneity under high-current density. Therefore, typical battery studies perform separate evaluations for coin and pouch cells. Voltage profile measurements of the CVD-Si electrode were conducted under low-current conditions for charging (i.e., 0.1C) and at a 5D discharge rate (see Figure 25a). The voltage profiles during charging and discharging appeared similar

between the two cell formats. Cycling tests were performed at a 1C charge rate for the coin cell and a 0.5C charge rate for the pouch cell, while both were discharged at a 5D rate. As shown in Figure 25b, the coin cell exhibited a higher specific discharge capacity than the pouch cell. However, the pouch cell demonstrated a slightly higher CE than the coin cell. Overall, both cells showed stable cycling performance for up to 150 cycles.

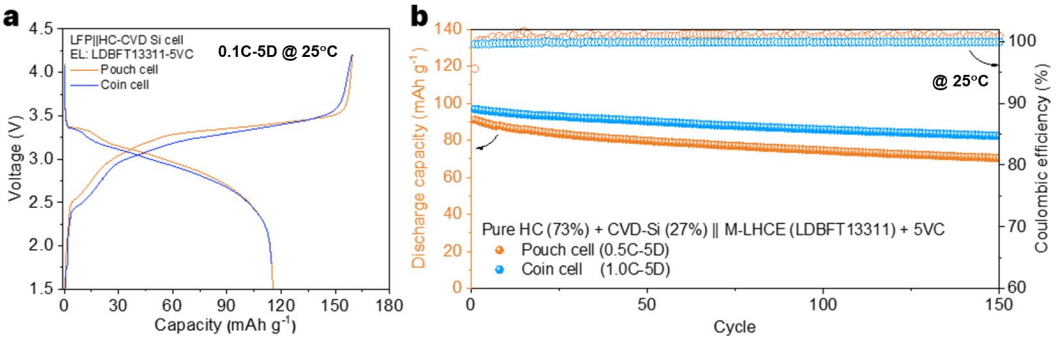

Figure 25. Pouch vs. coil cell performance of M-LHCE with CVD-Si composite anode at room temperature: a) voltage profiles at 0.1C formation and b) long-term cycle performance with 5D discharge rate.

4. Conclusions

Unlike ground vehicles, which are less sensitive to weight and size, UASs require higher power density to lift the airframe and its payloads, while being constrained by limited space. Higher power density necessitates higher discharge rates. Due to weight and size limitations, even greater discharge rates are needed to meet power density requirements. Simultaneously, UASs demand higher energy density to sustain range and endurance. These systems often operate under extreme conditions, such as very low temperatures. Therefore, UASs require energy storage solutions that deliver both high-power and high-energy density under harsh environmental conditions.

Current energy storage technologies, primarily developed for electric vehicles, perform poorly in extreme cold. Ground vehicles mitigate this with thermal management systems. However, implementing thermal management in UAS is challenging due to strict size and weight constraints. Moreover, thermal management consumes battery energy, further reducing range and endurance.

Si-anode batteries have garnered significant attention in recent years due to their high-energy density potential. However, their performance is limited by substantial volume expansion during cycling. This study explored the potential of Si-anode batteries by simultaneously optimizing anode and cathode active materials as well as electrolytes. CR2032 coin cells (Welcos) were used as the primary energy

storage format for most experiments, while a pouch cell was employed to assess the scalability of the developed materials. Charge rates of 0.5D and 1C were applied across all tests, with discharge rates ranging from 1D to 10D. Discharge rates were capped at 10D due to a significant decline in capacity. Even at 5D, a noticeable drop in discharge capacity was observed, with degradation beginning as early as 2D.

Although PC-NCM622 demonstrated higher specific discharge capacity than LFP across discharge rates from 1D to 10D, LFP exhibited much better relative capacity retention. Consequently, LFP was selected as the cathode active material. To optimize Si content in the anode, compositions ranging from 7 wt% to 30 wt% were evaluated. While ICE increased with higher Si content, electrode volume expansion rose exponentially beyond 15 wt%. Balancing ICE and volume expansion, 15 wt% was identified as the optimal Si content.

Electrolyte optimization focused on developing an LHCE capable of maintaining high ionic conductivity and stabilizing the SEI at low temperatures. Various combinations of LiFSI, DME, BME, FEC, and TTE, along with different solvent and diluent ratios, were investigated to evaluate performance at room temperature and –20 °C. Voltage profiles and specific discharge capacities across cycles were analyzed. Two formulations (C-LHCE and M-LHCE) were explored for low-temperature performance. M-LHCE, with reduced diluent and increased solvent content, maintained lower viscosity in cold conditions. FEC was added to enhance low-temperature behavior. M-LHCE showed improved specific discharge capacity at –20 °C but lower performance at room temperature compared to C-LHCE. EIS and DRT analyses revealed that FEC-containing electrolytes had lower charge-transfer resistance. Additionally, mesh-loaded electrode architectures demonstrated significantly lower resistance than pure HC electrodes.

After finalizing the electrolyte composition (i.e., LiFSI-DME-BME-FEC-TTE [LDBFT]), its variants were tested with 15 wt% and 30 wt% Si content. LDBFT (13311) and LDBFT (12411) emerged as the most promising, with LDBFT (13311) slightly outperforming the other. This formulation surpassed other state-of-the-art electrolytes reported in major journals under cold conditions.

Adding 5 wt% VC further enhanced long-term cycling stability at room temperature. To improve cold-temperature stability, CVD-Si was deposited onto porous HC. Results showed that HC and CVD-Si combined with M-LHCE and 5 wt% VC provided more stable cycling at low temperatures compared to the 15% Si reference electrode, although the reference electrode had higher specific discharge capacity.

The final Si-anode battery composition developed in this study consists of 73% HC, 27% CVD-Si, M-LHCE (LDBFT 13311), and 5 wt% VC. A pouch cell was fabricated to assess scalability, and voltage profiles along with long-term cycling tests confirmed consistent performance at room temperature.

This study successfully optimized cathode and anode active materials, electrolyte compositions, and electrode architecture to enhance the low-temperature performance of Si-anode batteries at high discharge rates. The resulting electrode outperformed existing Si-anode technologies under cold conditions. However, the developed battery is limited to discharge rates below 2D at –20 °C to maintain capacity retention comparable to room temperature. At –20 °C, capacity retention drops to approximately 28% of the initial capacity, which is insufficient for UAS applications that demand high payload, extended range, and long endurance. To be viable for UASs, the Si-anode battery must incorporate thermal management, though this introduces trade-offs in payload and range. The most effective application for this battery is within a hybrid electric propulsion system that includes thermal regulation and restricts extreme operational conditions to short durations.

5. References

1. Dixit M et al. Lithium-ion battery power performance assessment for the climb step of an electric vertical takeoff and landing (eVTOL) application. ACS Energy Letters. 2024;934–940.
2. Nitta N, Wu F, Lee JT, Yushin G. Li-ion battery materials: present and future. Materials Today. 2015;5:252–264.
3. Choi JW, Aurbach D. Promise and reality of post-lithium-ion batteries with high energy densities. Nature Reviews Materials. 2016;1.
4. Bommier C, Surta TW, Dolgos M, Ji X. New mechanistic insights on Na-ion storage in nongraphitizable. Nano Letters. 2015;15:5888–5892.
5. Xie L et al. Hard carbon anodes for next-generation Li-ion batteries: review and perspective. Advanced Energy Materials. 2021;11. https://doi.org/10.1002/aenm.202101650
6. Casimir A et al. Silicon-based anodes for lithium-ion batteries: effectiveness of materials synthesis and electrode preparation. Nano Energy. 2016;27:359–376.
7. Zhang X et al. Stable high-capacity and high-rate silicon-based lithium battery anodes upon two-dimensional covalent encapsulation. Nature Communications. 2020;11:3826. https://doi.org/10.1038/s41467-020-17686-4
8. Hubble D et al. Liquid electrolyte development for low-temperature lithium-ion batteries. Energy & Environmental Science. 2022;15:550–578.
9. Xu K. Electrolytes and interphases in Li-ion batteries and beyond. Chemical Reviews. 2014;114:11503–11618.
10. Cao X, Jia H, Xu W, Zhang J-G. Review—localized high-concentration electrolytes for lithium batteries. Journal of The Electrochemical Society. 2021;168.
11. Lu D et al. Ligand-channel-enabled ultrafast Li-ion conduction. Nature. 2024;627:101–107.
12. Xu J et al. Electrolyte design for Li-ion batteries under extreme operating conditions. Nature. 2023;614:694–700.
13. Gao Y et al. Low-temperature and high-rate-charging lithium metal batteries enabled by an electrochemically active monolayer-regulated interface. Nature Energy. 2020;5:534–542.

14. Zhang G et al. A monofluoride ether-based electrolyte solution for fast-charging and low-temperature non-aqueous lithium metal batteries. Nature Communications. 2023;14:1081.

List of Symbols, Abbreviations, and Acronyms

Al	aluminum
BME	butyl methyl ether
C	charge rate
CE	coulombic efficiency
C-LHCE	conventional-LHCE
Co	cobalt
Cu	copper
CVD	chemical vapor deposition
D	discharge rate
DME	1,2-dimethoxyethane
DRT	distribution relaxation time
EIS	electrochemical impedance spectroscopy
FEC	fluoroethylene carbonate
HC	hard carbon
ICE	initial coulombic efficiency
LFP	lithium iron phosphate
LHCE	localized high-concentration electrolyte
Li	lithium
LIB	lithium-ion battery
LiFSI	lithium bis(fluorosulfonyl)imide
mAh	milliampere-hour
M-LHCE	medium-LHCE
Mn	manganese
NCM	nickel cobalt manganese
Ni	nickel
NMC	nickel manganese cobalt

PAA	poly(acrylic acid)
PC	polycrystalline
PE	polyethylene
PVdF	polyvinylidene fluoride
SC	single crystalline
SEI	solid-electrolyte interphase
SEM	scanning electron microscopy
Si	silicon
SWNT	single-walled carbon nanotube
TTE	1,1,2,2-tetrafluoroethyl-2,2,3,3-tetrafluoropropyl ether
UAS	unmanned aircraft system
VC	vinylene carbonate
wt%	weight percent

1 (PDF)	DEFENSE TECHNICAL INFORMATION CTR DTIC OCA
1 (PDF)	DEVCOM ARL FCDD RLB CI TECH LIB